Graphical abstract

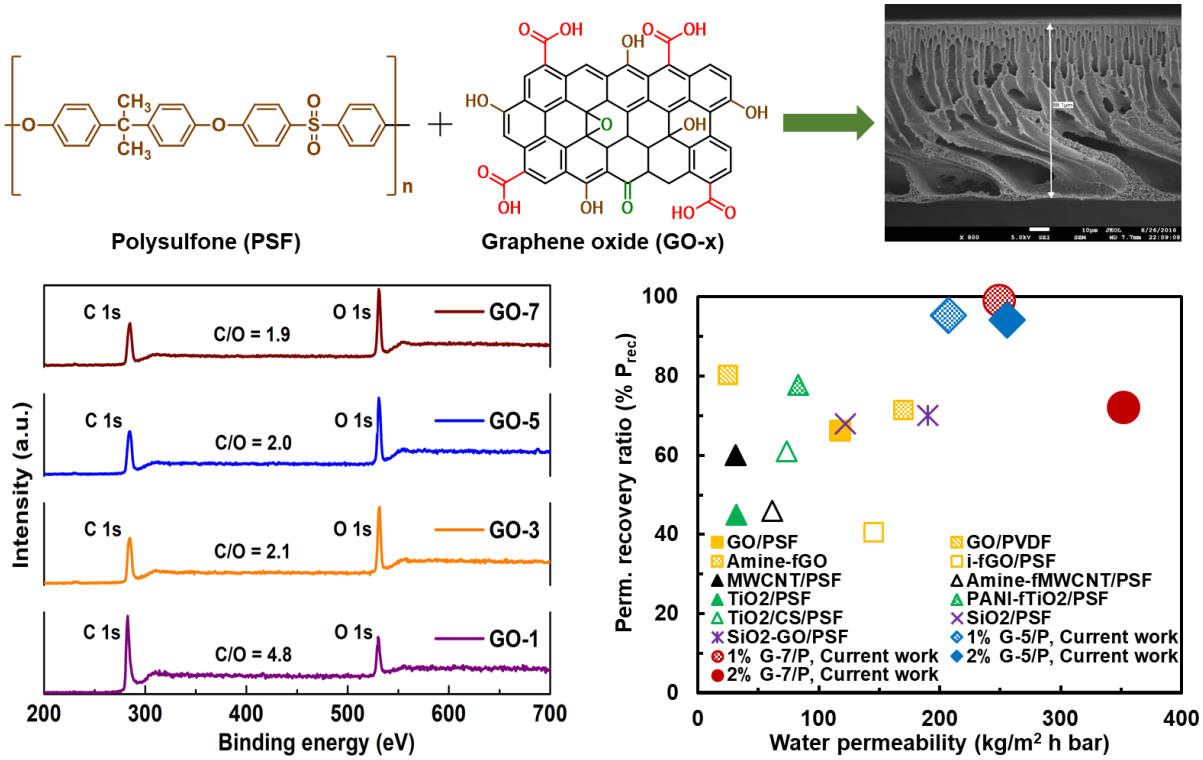

Effect of oxidation degree of GO nanosheets on microstructure and performance of polysulfone-GO mixed matrix membranes

Rahul S. Zambare[a,1], Kiran B. Dhopte[a], Parag R. Nemade[a,b,*], Chuyang Y. Tang[c]

[a] Department of Chemical Engineering, Institute of Chemical Technology, Mumbai, India 400 019

[b] Department of Oils, Oleochemicals and Surfactant Technology, Institute of Chemical Technology, Mumbai, India 400 019

[c] The University of Hong Kong, Department of Civil Engineering, Pokfulam, Hong Kong

[*] Corresponding author: P. R. Nemade; Tel.: + 91- 22 3361 2027; Fax: +91- 22 3361 1020. E-mail: pr.nemade@ictmumbai.edu.in

[1] Current Address: Centre for Advanced 2D Materials, National University of Singapore, Singapore-117 546

Abstract

Graphene oxide with increasing degree of oxidation (GO-x) were incorporated in polysulfone (PSF) mixed-matrix ultrafiltration membranes. Synthesized GO-x were characterized for average particle size by AFM and DLS method; oxygen functionalities and nanostructure properties by XPS, FT-IR, XRD, Raman analysis, TEM, and elemental analysis; surface charge by zeta potential. Increasing oxidation degree, increased the proportion of carbonyl functional groups, exfoliation, lowered zeta potential and particle size in GO. GO-x with higher oxidation degree showed significantly improved dispersibility in N-methyl-2-pyrrolidone and polysulfone matrix. Blending hydrophilic GO-x, enhanced phase-separation kinetics improving porosity, tensile strength, permeability, protein rejection, and fouling resistance of membranes. With the increase in the oxidation degree of the matrix, contact angle and surface charge on the membranes decreased. 2%-GO-7/P membrane showed permeate flux of 352 $kg.m^{-2}h^{-1}bar^{-1}$ while, 1%-GO-7/P membranes acquired permanent negative charge and displayed permeability of 250 $kg.m^{-2}h^{-1}bar^{-1}$ with BSA rejection of about 97 %, compared to control membrane permeability of 102 $kg.m^{-2}h^{-1}bar^{-1}$ with BSA rejection of about 91 %. Thus, the membrane flux-rejection trade-off is overcome. 1%-GO-7/P membrane displayed exceptional flux recovery of over 99 % on simple DI water flushing. The superior performance of GO-x/P membranes is attributed to faster diffusion rate of water across GO matrix over that through the polymer solution, which increased the number of thermodynamic instabilities giving higher rate of phase inversion resulting in narrow pore size distribution and higher pore density, demonstrating simple approach for enhancing performance of UF membranes.

Keywords: graphene oxide; different oxidation states; mixed matrix membranes; ultrafiltration; structure; performance;

1 Introduction

With the industry evolution, modern membrane technology is becoming more prominent in separation processes [1,2]. Membrane selectivity and permeability are two important aspects for membrane-based separations [3,4]. In the core of membrane applications, ultrafiltration (UF) process is widely used in chemical and pharmaceutical industries, water purification, food and beverage processing, dialysis and gas separations [1,2,5–7]. The membrane morphology and internal structure of polymeric UF membranes synthesized by phase inversion are intricately linked to the properties of the polymer, additives, dope solution, temperature, external moisture, etc. [8]. Two important forces act on the film during the process of phase inversion. The thermodynamic instabilities generated due to the mixing of solvent and the non-solvent causing precipitation of the polymer. If these instabilities are generated and propagated quickly, a membrane with a thin top layer is formed. Countering the propagation of thermodynamic instabilities is the viscous forces limiting solvent-non solvent mixing. A membrane with a thick top layer is generated when hindrance to solvent-non solvent mixing due to viscous dope solution predominates thermodynamic instabilities. These phenomena give rise to flux-rejection trade-off [8–11].

The performance of asymmetric polymer membranes can be improved by the addition of an external matrix such as nanoparticles [12]. The addition of an external matrix to the polymer dope solution changes the dynamics between viscous hindrance and lower the thermodynamic stability. These hybrid membranes overcome the flux-rejection trade-off. In hybrid or mixed-matrix membranes, the thermodynamic instabilities are also created at the phase boundary of the solid matrix and the polymer solution. De-mixing is accelerated due to hydrophilic matrices. Nanoparticle additives are particularly effective in improving the performance of the membranes due to high surface area, ease of dispersion, and mobility [13]. Another benefit of hydrophilic matrices is the lowering of water contact angle of the

membrane, which further decreases membrane resistance to water ingress giving better water flux and improving resistance to fouling due to the deposition of hydrophobic moieties [12,14].

Graphene oxide (GO), a stacked two-dimensional carbon nanomaterial with hydrophilic functionalities, is a particularly effective matrix [15]. The d-spacing between the graphite layers is higher in GO, in comparison to graphene and graphite, due to defects and oxygen functionalities on the surface and the edges of the graphitic sheets [16]. GO has a high specific surface area; good mechanical stiffness and water can travel rapidly between the layers than diffuse through the viscous polymer matrix triggering polymer precipitation at the edges of the GO sheets giving finely porous membranes with both high flux and high rejection [17,18].

GO platelets blended during dope solution raise the viscosity. Studies reported limitation on GO loading in membrane dope solution, beyond which, the performance degrades. A higher concentration of GO also presents issues in dispersion and suppresses membrane performance [19,20]. GO sheets with low zeta potential due to oxygen functionalities are stable [16]. GO sheets with a high degree of oxidation show increased d-spacing, and the sheets have a much lower tendency of aggregation, indicating repulsive forces due to oxygen functionalities [21]. A dispersion of such GO with a high degree of oxygen functionalities can overcome limitation membrane performance due to the high viscosity of membrane solution [22,23]. A control on these properties for other nanomaterials is difficult but is possible in GO. The zeta potential of GO can be tuned by controlling the oxidation of GO. The changes in the oxidation degree of GO produce changes in oxygen functionalities on the basal plane and edge of the nanosheet [24–26]. The effect of zeta potential of the matrix on the viscosity, hydrophilicity, morphology, and performance of the membrane is lacking [12]. A study of variation in morphology, properties, and performance of the membranes with changes in zeta potential, hydrophilicity, as well as the concentration of matrix in dope will give insights on the development of high-performance membranes.

Herein, we report a systematic study on the effect of GO with varying oxidation degree (GO-x) on the microstructure and performance of the resultant GO-x blended polysulfone (PSF) mixed matrix membrane. GO-x were synthesized by varying the proportion of oxidant, $KMnO_4$, during synthesis. The changes in GO with different oxidation degree were determined by observing variation in d-spacing, functional groups, proportion of functional groups, defects and variation of GO stacks, dispersion stability and zeta potential. The membranes were synthesized by casting a blend of GO-x in polymer dope solution, as well as changing the concentration of GO-x in the dope solution followed by phase inversion. The structural, hydrophilicity, permeability, BSA rejection, fouling resistance, and mechanical properties of membrane were analysed to evaluate the effect of GO with varying oxidation degree. The role of oxygen-containing functional groups and the average particle size of GO-x in mixed matrix membrane is also discussed. Two trends are analyzed, the effect of increasing oxidation degree of GO, and the effect of increasing loading of GO-x on the membrane properties.

2 Experimental

2.1 Materials

Polysulfone (Udel 1700, Solvay Chemicals) was used for casting membranes. N-methyl-2-pyrrolidone (NMP, SD Fine Chemicals) was used as a solvent to dissolve polysulfone and other additives. Graphene oxide (GO) was synthesized from natural graphite powder (325 mesh, Alfa Aesar). Sulfuric acid (H_2SO_4), potassium permanganate ($KMnO_4$), sodium nitrate ($NaNO_3$) (SD Fine Chemicals) were used to oxidize natural graphite to form graphene oxide. Poly(ethylene glycol) (PEG-400, average molecular weight: 400 g/mol, SD Fine Chemicals) was used as pore-forming agent. Deionized (DI) water was used as the non-solvent in the phase inversion process. 1000 mg/L BSA solution (molecular weight: 66 kDa, HiMedia) was

prepared in phosphate buffer saline (1x PBS, 10 mM, pH = 7.4) and used to study the antifouling performance of the membrane.

2.2 Synthesis of different oxidation degree graphene oxide (GO-x)

Graphene oxide was prepared by the modified Hummers method [24,27,28]. A detailed procedure of the synthesis of GO-x is given in Supporting Information (Figure S1). GO samples with increasing oxidation degrees are denoted as GO-1, GO-3, GO-5, and GO-7, respectively, according to the amount of the $KMnO_4$/graphite mass ratio.

2.3 Preparation of GO-x/polysulfone mixed matrix membrane

Membrane solutions were prepared by mixing PSF (15 wt %) in NMP, 10 wt % PEG-400 and GO-x. GO-x-polysulfone mixed matrix membranes were synthesized using non-solvent induced phase separation (NIPS) method. Briefly, GO-x was dispersed in NMP using sonication for 2 h, while maintaining the water temperature below 35 °C in the sonication bath. PSF was dried at 100 °C for 4 h to remove surface moisture. PSF and PEG-400 were added to the GO suspension under stirring at room temperature, and the mixture was subjected to heating at 60 °C for 24 h to obtain a homogeneous dope solution. Before the membrane casting, entrapped air bubbles/gases in dope solution were removed by sonication for 1 h, and the solution was kept still for 12 h. The solution was cast on a clean glass plate using a film applicator for a wet film thickness of 200 µm. The glass plate was then immersed in a coagulation bath containing DI water at room temperature for 30 min to induce phase inversion giving porous asymmetric PSF membrane. This membrane was transferred to another DI water bath for 24 h to ensure complete phase reversal. Subsequently, the membranes were stored in wet condition under DI water

until further use. Membranes are denoted as 'a% GO-x/P', where 'a' is the weight percent of GO based on PSF mass, 'x' is the oxidation degree of GO and P is the 10 wt% of PEG-400 based on the mass of the mixture.

2.4 Characterization of GO-x

Average particle size and zeta potential of GO-x (100 mg/L aqueous dispersion) were analyzed using dynamic light scattering (DLS) method (Zetasizer Nano ZS90, Malvern Instruments). Average flake size and flake size distribution of GO-x were determined from Atomic Force Microscopy (AFM, Dimension Fastscan, Bruker) images. Fourier Transform Infrared Spectroscopy (FT-IR, Spectrum BX, Perkin Elmer) was used to determine various functional groups exist on GO-x. Crystalline nature and interlayer distance between graphene sheets were identified by X-ray diffractometer (XRD) (D8 ADVANCE, Bruker) equipped with Cu K_α radiation (λ=1.5406 Å). Defects and disorder in GO-x were determined by Raman spectrophotometer (HR-800, Horiba Scientific). Crystallite size was calculated using I_D/I_G ratio. Quantitative analysis of surface functional groups present on GO-x was evaluated using X-ray photoelectron spectroscopy (XPS) (PHI 5000 Versaprobe II, ULVAC-PHI) equipped with monochromatic Al K_α excitation radiation. Quantitative composition of elements in GO-x was determined by CHNSO analyzer (FLASH EA 1112, Thermo Finnigan). Morphology and micro-structure as well as the electron transparency nature GO nanosheets was analyzed using High Resolution Transmission Electron Microscopy (HR-TEM, JEOL) at an operating voltage of 300 kV.

2.5 Characterization of membranes

Change in casting solution viscosity at the different shear rate (10 to 100 s^{-1}) was measured using rheometer (Physica MCR 301, Anton Paar) at 25 °C to study the effect of GO-x on the viscosity of the casting solution and membrane formation process. The surface and cross-sectional morphologies of GO-x/PSF membranes were analyzed by a field emission electron microscopy (FE-SEM, JSM-6400, JEOL). For SEM sample preparation, small pieces of membrane sample were dipped into liquid nitrogen and were fractured by a pair of tweezers. Fractured samples fixed to the SEM sample holder and coated with a thin layer of platinum. The average pore size and pore size distribution of GO-x/P membrane were determined from SEM surface micrographs using 'ImageJ' using procedure described else where [20]. Overall porosity (ε) was calculated by measuring the weight and the thickness of the membrane of known area in fully hydrated and desiccated conditions. The membrane specimens were dried in a vacuum oven at 100 °C for 24 h and weighed (w_d). Then, membrane specimens were soaked in DI water for 30 h to get constant mass (w_w); wiped with tissue paper quickly and thickness and mass were subsequently measured to calculate overall porosity using equation (1);

$$\% \ \varepsilon = \frac{W_w - W_d}{\rho_{H_2O} \times \Delta x \times A} \times 100 \qquad (1)$$

where ρ_{H_2O} is the density of water (996 kg/m^2), Δx is membrane thickness (m), and A is effective membrane area (m^2). Overall porosity was measured in triplicate using three membrane samples, and the average value is reported. Membrane water contact angle was measured at 25 °C using sessile droplet method (G10, Kruss) to estimate the hydrophilicity of the membranes. Membrane samples were wiped with tissue paper and kept at 40 °C under vacuum for 12 h to remove surface moisture. Water droplet (~ 1 µL) was dropped by vertically aligned micro-syringe on the membrane surface, and the contact angle was measured by adjusting a tangent to the droplet. A minimum of 10 measurements was made for contact angle at different places for each membrane, and the average value is reported.

Membrane surface charge was analyzed by a ζ-potential analyzer (SurPASS, Anton Paar) with a 1 mM NaCl solution circulated through the adjustable gap cell (20 mm × 10 mm). 0.05 M HCl and 0.05 M NaOH solutions were used to adjust the pH of the electrolyte solution in order to monitor the ζ-potential change at different pH values. Mechanical properties of the membranes were evaluated by measuring tensile strength (Model 3366, Instron Universal Materials Testing Machine). For measurement, 100 mm × 15 mm rectangle shape membrane specimens (3 numbers) having thickness ~ 90 µm were dried at room temperature for 12 h. Tensile strength was performed with a stretching rate of 1 mm/min using 250 N load cell keeping 30 mm initial distance between two jaws.

2.6 Membrane permeability and rejection studies

Membrane permeability and rejection experiments were carried out in a custom-designed cross-flow filtration cell with 9.75 cm^2 effective filtration area. The permeate volume was monitored using electronic weighing balance interfaced to a computer. Each membrane was pre-compacted using DI water permeation at 3 bar transmembrane pressure for 180 min to attain steady permeate. Transmembrane pressure was reduced to 1 bar and permeate was collected over another 100 min. Permeate weight was recorded for every 1 min to obtain permeability versus time plot. Average DI water permeability, P_w^i (kg/m^2 h bar) of the membrane is calculated using equation (2);

$$P_w^i = \frac{\Delta \mathrm{w}}{A \times \Delta t \times \Delta \mathrm{P}} \qquad (2)$$

where Δw is the permeate weight measured (kg), A is the effective area of membrane (m^2), Δt is permeation time (h), and ΔP is trans-membrane pressure.

Then, DI water was replaced by 1000 mg/L BSA solution and was filtered through the membrane at 1 bar trans-membrane pressure for 100 min. The permeate weight was recorded, and BSA solution

permeability (P_{BSA}) was estimated. BSA concentration in feed and permeate solution was estimated using the Bradford method and the rejection of BSA (*% R*) was calculated using equation (3):

$$\% R = \left(1 - \frac{C_p}{C_f}\right) \times 100 \quad (3)$$

where, C_p and C_f are the concentrations of BSA in permeate and feed, respectively.

After membrane fouling with BSA, membranes were flushed with DI water for 10 min in situ. Recovered DI water permeability (P_w^f) was measured under the same operating conditions as used earlier during DI water permeability measurement, and permeability recovery ratio (% P_{rec}) was calculated using equation (4);

$$\% P_{rec} = \frac{P_w^f}{P_w^i} \times 100 \quad (4)$$

Higher the permeability recovery ratio (% P_{rec}) better is the antifouling property of the membrane. In order to understand fouling behavior, reversible fouling ratio ($\% R_r$) and irreversible fouling ratio ($\% R_{ir}$) were calculated using the following equations (5) and equations (6);

$$\% R_r = \frac{P_w^f - P_{BSA}}{P_w^i} \times 100 \quad (5)$$

$$\% R_{ir} = \frac{P_w^i - P_w^f}{P_w^i} \times 100 \quad (6)$$

3 Results and discussions

3.1 Characterization of GO-x

C 1s spectra of GO-x deconvoluted into three peaks at 284.8 eV, 286.9 eV and 288.2 eV attributed to signals of sp^2-hybridized C-C, C-O (hydroxyl and epoxy) and C=O (carbonyl), respectively as shown in Figure 1. C 1s spectra of GO-1 shows two peaks; one distinct peak of sp^2-hybridized carbon (C-C) and for (C-O) groups with a negligible amount of (C=O) groups which signify a lower degree of oxidation. With increasing oxidation (GO-3 to GO-7), the peak intensity of sp^2-hybridized C-C decreased relative to oxygen-containing functional groups (hydroxyl, epoxide, and carbonyl). the intensity of sp^2-hybridized carbon (C-C) decreased with increasing intensity of peaks attributed to (C-OH) and (C=O) groups respectively. Table S1 summarizes the proportion of deconvoluted peaks due to oxygen-containing functional groups. The proportion of carbonyl functional groups (C=O) increases from 1.2 % in GO-1 to 13 % in GO-7 confirming an increase in the oxidation level. In Figure S2, the XPS survey spectrum of GO-x shows two intense characteristic peaks of C 1s and O 1s. A decrease in C/O ratio from 4.8 to 1.9 was seen in the spectra of resulting GO with an increase in $KMnO_4$ used per gram of natural graphite, confirming the increase in oxidation levels from GO-1 to GO-7 (Table S1).

The FT-IR spectrum of GO-1 showed a band at 1580 cm^{-1} due to the presence of C–C stretching in the graphitic domain along with weak absorption band at 3426 cm^{-1} of a hydroxyl group (-OH) demonstrating a lower oxidation level (Figure 2a)., FTIR spectra showed additional oxygen-containing functional groups such as C=O (1725 cm^{-1}), C–O (1057 cm^{-1}), C–O–C (1221 cm^{-1}) and C–OH (1400 cm^{-1}) in the GO-x samples supporting the XPS spectra with the increase in oxidation level. A broad peak around 3426 cm^{-1} was attributed to -OH stretching due to the presence of absorbed moisture. FT-IR spectra of GO-3, GO-5, and GO-7 looked very similar to each other, exhibiting the same functional group's bands. However, the relative intensity of bands was remarkably changed that shows the presence of increased

chemical functionalities on GO-x. Increase in oxidation level of GO-3, GO-5, and GO-7 showed the strongest band at 1725 cm^{-1} that confirmed the presence of a large number of carboxylic acid groups found in XPS analysis.

Further, XRD analysis provides information about crystallinity, oxidized, and un-oxidized regions in GO-x (Figure 2b). Natural graphite XRD spectra showed an intense peak at 2θ = 26.7° corresponding to (002) diffraction plane in hexagonal carbon structure having an interlayer (d) spacing of 0.32 nm. GO-1 spectra show two peaks, hexagonal graphitic plane (002) at 2θ = 26.5°, d = 0.35 nm and defected hexagonal graphitic plane (001) at 2θ = 14.5°, d = 0.61 nm due to partial oxidation of graphitic carbon surface. Comparing diffractograms of GO-3, GO-5 and GO-7, the hexagonal graphitic plane about 2θ = 26.5° completely disappeared and a new and prominent peak (001) due to the insertion of oxygen-containing functional groups on the graphitic lattice appeared in the range of 2θ = 9.9 to 10.4°. With the increase in oxygen-containing functional groups in GO-3, GO-5 and GO-7, the (001) peak shifted to a lower angle (2θ = 10.4°, 10.1°, and 9.9°) giving an interlayer spacing of 0.85 nm, 0.88 nm, and 0.89 nm, respectively. Increased interlayer spacing would help to improve the dispersion of GO-x in the membrane casting solution.

Raman spectroscopy was used to determine the defects, bond length, vacancies, disorders, presence of sp^2 and sp^3 domains on the graphitic lattice and crystallite size of GO-x. In Figure 2c, the Raman spectra of all GO-x (laser excitation source of 514.5 nm) showed two intense characteristic bands; ~ 1575 cm^{-1} assigned to the G band corresponding to vibrational E_{2g} mode for sp^2 carbon atoms; ~ 1330 cm^{-1} assigned to the D band corresponding to A_{1g} mode that appears from the defects in graphitic lattice and boundaries of crystallites. Raman spectra of natural graphite showed sharp peaks for G-band that arises from the plane vibration of sp^2-hybridized carbon atoms and no significant D-band that would identify defects and sp^3-hybridized bonds indicate the high crystallinity and defect-free graphite layer. Natural graphite spectra show another feature peak at 2700 cm^{-1} called 2D band (G' band); overtone of the D

band. After oxidation of graphite, the 2D peak at 2700 cm^{-1} disappeared, and a prominent D band appeared. On mild oxidation to GO-1, the intensity of D-band increased surpassing the intensity of G-band as a result of the defects induced during partial oxidation. As the oxidation increased blue shift of G-band peak is observed from a wavenumber of 1566.3 cm^{-1} to 1589.5 cm^{-1} for the samples from GO-1 to GO-7, respectively. The shift in G band is associated with the formation of new sp^3 carbon atoms and the insertion of oxygen functionalities (hydroxy, epoxy, and carboxyl) on the surface and the edges of the graphitic lattice.

Similarly, the different oxidation degree affects the nature of the D band. The full-width half maxima (FWHM) increases from 75 to 108.2 cm^{-1} for GO-1 to GO-7 respectively with increasing the oxidation degree. The presence of the D-band in the Raman spectra and its magnitude for GO-x revealed increasing oxygen-containing functional groups on the graphitic lattice, which is also in agreement with XPS and FT-IR analyses. I_D/I_G ratio decreases with the increase in oxidation degree of GO-x. GO-1 shows high I_D/I_G ratio of 1.20, whereas at higher oxidation degree GO-3 to GO-7 gives (I_D/I_G) ratio as 1.11, 1.04, and 1.06, respectively. The slight increase in I_D/I_G ratio at the highest oxidation level in GO-7 is due to the broad nature of G band.

Further, In-plane sp^2 crystallite size (L_a) of GO sheets was calculated from the correlation between the I_D/I_G ratio and the wavelength of the laser source (λ_1, nm) used in the measurement [29]. The equation is given as;

$$L_a = \frac{2.4 \times 10^{-10} \cdot (\lambda_1)^4}{[I_D/I_G]} \quad (4)$$

The calculated L_a values are shown in Table S2. L_a value of natural graphite is calculated to be 64.1 nm. The average crystallite size increased with an increase in oxidation degree of GO; this may be due to the change in crystallinity, the formation of additional defects, disorder, sp^3-hybridization. In GO-7, L_a

slightly decreased at higher oxidation degree, which is in agreement with previously reported crystallite size of GO at different oxidation degree [25,30]. Overall, Raman analysis gave evidence of the conversion of crystalline graphite into oxygenated graphene oxide through the disruption of graphite stacks with increased degree of oxidation.

The GO sheets will acquire negative charge on the dissociation of electronegative oxygen containing functional groups in solution. Therefore, a decrease in the zeta potential of GO suspension indicates the uniform distribution of functionality and an increase in oxygen-containing functional groups. The zeta potential of the suspensions was negative as was expected. The zeta potential of GO-aqueous dispersion (Figure 2d) showed a monotonic increase in the amplitude of the zeta potential with an increase in the oxidation degree. Higher negative zeta potential of GO-x indicates highly hydrophilic nature of GO nanosheets. GO-7, with the highest oxidation degree, possesses the most negative zeta potential owing to greater incidence of carbonyl groups, as supported through XPS analysis.

The morphology and micro-structure of GO-x nanosheets was analysed by TEM (Figure 3). A change in the layer structure is observed as the extent of oxidation increases in GO. In lowest oxidized GO-1, aggregated particles and dark areas indicate the thick stacking nanostructure consisting of several graphitic layers. The TEM of GO-3 sheets depicts multi-layered lamellae that are better exfoliated than GO-1. Some crumpling of GO-nanosheets is also observed. On the other hand, GO-5 and GO-7 images show largely transparent artifacts indicating thinner films, and greater exfoliation. At highest oxidation in GO-7 TEM image shows smooth and significantly large surface area of high transparency delaminated GO nanosheets. Increased number of oxygen functionalities on GO results in increased exfoliation on sonication. Comparison of selected area electron diffraction pattern of GO-x reveals changes in crystallinity. In GO-1, multiple spots are observed. The spots indicate sharp diffraction peaks arising due to highly crystalline structure. As the extent of oxidation increases, the spots disappear and a broad ring-

like pattern is observed. A sharp ring indicates polycrystalline sample, while broad ring indicates nanodimensional polycrystalline samples.

Particle size distribution was determined by Atomic Force Microscopy (AFM) imaging (Figure 3) and dynamic light scattering (DLS) methods based on the Stokes-Einstein equation. DLS provides hydrodynamic particle size, which is expected to be close to the lateral dimension of GO nanosheets [32]. AFM images were processed in Gwyddion to correct for drifts during scanning [33]. Then, each image was edited in ImageJ and flakes were selected by masking the thresholded area. Finally, the Feret's statistical diameter were determined by analysing each masked flake. Feret's statistical diameter was further considered as a flake size [34], and were compared with DLS average particle size. The size distribution of GO-x nanosheets is shown in Figure 3.The change in the average flake size of GO nanosheets as a function of different oxidation degree is shown in Table S2. The average size of the flakes obtained by AFM and DLS show good agreement. The change in the DLS average particle size of GO nanosheets as a function of different oxidation degree is shown in Table S2. At the lowest oxidation degree, GO-1 showed the largest average particle size of 810 nm due to limited exfoliation of graphitic oxide. The particles size reduced in GO-3 and GO-5 to 323 nm and 210 nm, respectively. Further, the average particle size of GO-7 increases marginally to 259 nm. GO nanosheets with the exception of GO-1 show good dispersion in solution and self-stabilize suspensions both in water and in dope solution (Figure S3). Lower size with higher oxygen percentage is attributed to cleavage and defect formation during the oxidation process. At the highest oxidation degree, π-conjugation in GO-7 may be low due to the abundant oxygen-functional groups and more defect sites. Lower π-conjugation decreases the viscosity of the suspension and translational diffusion coefficient that results in a slight increase in hydrodynamic diameter of GO sheets [35].

The elemental analysis of the GO-x after oxidation supported changes in the atomic composition expected with the increase in the degree of oxidation. The content of each element in GO-x summarized

in Table S2 shows that the carbon content of a GO-x decreased in order to 83.2 (GO-1) > 58.3 (GO-3) > 55.4 (GO-5) > 48.9 (GO-7) that shows a decrease in graphitic domains with increasing oxidation level. The oxygen content of GO-x increased in the order of 14.6 (GO-1) < 39.3 (GO-3) < 41.6 (GO-5) < 47.8 (GO-7), indicating that additional oxygen-containing functional groups were generated on GO sheets during synthesis with increasing $KMnO_4$ content. The degree of oxidation of GO-x is directly proportional to the amount of oxidizing agent used during oxidation.

3.2 Characterization of membranes

The viscosity of dope solution has a significant impact on the membrane parameters such as rate of exchange between solvent and non-solvent during the phase inversion, membrane thickness, and skin integrity [20]. Change in membrane structure and morphology influences the performance of the asymmetric membranes. To understand the effect of GO at different oxidation degree on membrane dope solution, change in viscosity at various shear rates was studied (Figure 4). The rheological characteristics of the casting solution did not change notably with the increase in the shear rate, indicating the Newtonian character of dope solution with 1 wt% of GO-x (Figure 4a). The viscosity of the solutions containing 1 wt% of GO-3 and GO-5 did not vary significantly compared to control casting solution without blending of GO-x. The solution containing 1 wt% GO-7 showed the lowest viscosity that can be attributed to a reduction in π-conjugation due to the presence of larger number of oxygen-functionalities and defects during oxidation. Abundant oxygen-functionalities present at the edges and on the plane of the graphene oxide interact with PEG by hydrogen bonding and intercalating PEG between the GO sheets. This highly hydrophilic PEG intercalated GO form the non-covalent interactions with oxygen-containing functional groups on PSF, disturb the parent matrix of PSF forming a low shear strength structure [36,37]. The casting solution viscosity increased marginally with an increase in the

amount GO-x to 2 wt% (Figure 4b). Further, casting solution containing GO-5 with same oxidation degree at different loading from 1 w% to 5 wt% displayed a gradual increase in viscosity shown in Figure 4c. The viscosity of casting solution containing 1 wt% and 2 wt% of GO-5 was almost constant at different shear rates. Whereas, the viscosity of casting solution containing 5 wt% GO-5 decreased by almost 35% on a 10-fold increase in shear rate. It indicates that the rheological properties of the casting solution change from Newtonian to pseudoplastic behavior with the increase in GO loading. The shear-thinning behavior of casting solution containing 5 wt% of GO-5 is attributed to the stacking of GO sheets due to strong π-π conjugate interactions. These stacks cause an increase in the free volume of casting solution. The stacks are disrupted at higher shear rate due to the distraction of GO sheets resulting in lower viscosity of the casting solution [20]. The casting solution viscosity at 10 s^{-1} shear rate of the fabricated membranes is shown in Table 1. During the phase inversion process, polymer precipitation starts at the top interface of the wet film that forms smaller pores and a more selective skin layer. The top layer hinders further mixing of the solvent in the casted film and the non-solvent from the bath. Crystallization occurs gradually as the non-solvent diffuses from the skin layer. These dynamics contribute to the formation of a finger-like structure in the bottom layer. An increase in casting solution viscosity depresses the diffusion rate between the solvent and the non-solvent. Therefore, an increase in the viscosity of dope solution leads to the formation of a dense-skinned top layer and the finger-like structure growth widely in sub-layer that get mixed with bottom spongy layer after completion of the phase inversion.

Figure 5 shows the changes in the morphology of the membrane with the addition of GO-x. The cross-section image of 10 wt% PEG membrane, synthesized without any GO-x, shows asymmetric structure typical of phase inversion synthesized membrane, a skin layer that acts as a separating layer, porous sub-layer containing finger-like micro-voids beneath, and a sponge-like surface at the bottom. The internal structure of the membrane is altered significantly due to the presence of GO-x stacks in the

polymer matrix. The finger-like pores become longer and broader with increasing the oxidation degree of GO-x for both 1% GO-x/P and 2% GO-x/P membranes. Whole finger-like pores in sub-layer changes to little suppressed finger-like pores and merged with the spongy structure at the bottom surface. 1% GO-3/P membrane shows a thin selective top layer whereas, at 2% GO-3/P membrane shows thicker and less porous skin layer. It suggests that increased viscosity of casting solution of 2% GO-3/P membrane is a rate-limiting factor during the phase inversion process due to lower hydrophilicity of GO nanosheets at lower oxidation degree. As oxidation degree of GO-x increases, 2% GO-5/P and 2% GO-7/P membranes show thin selective top layer signifying that hydrophilicity is a rate-limiting factor in the phase inversion process. For GO-5 blended membranes, on increasing the content of GO, width and length of finger-like pores first increase and then decreases indicating an optimum threshold of GO for maximum voidage. At highest oxidation degree in GO-7, both 1% GO-7/P and 2% GO-7/P membrane show thin selective top layer and interconnected finger-like pores due to the low viscosity of casting solution as well as an increase in hydrophilicity of GO nanosheets. The threshold is 1 wt% of the GO-3 and 2 wt% of GO-5 and GO-7 in the dope solution respectively. The overloading of GO-x significantly increases the casting solution viscosity giving a dense top layer that hinders the diffusion of solvent in to the non-solvent during the process of phase inversion.

The surface image of 10% PEG membrane synthesized without the addition of GO-x, shows the presence of small pores. It shows a narrow pore size distribution with an average pore size of 2.7 nm. The overall porosity of the membrane surface increases in 1% GO-x/P membrane compared to control 10% PEG membrane. The surface of 1% GO-7/P membrane shows a porous structure that indicates the influence of oxygen-containing functional groups in GO-7 on the structure of the membrane. At 1% GO-x/P membrane, the order of average pore size of the membrane with the different oxidation level follows, 3.9 nm (GO-3) > 3.7 nm (GO-7) > 3.2 nm (GO-5). The change in order of pore size distribution and average pore size of membrane very well match with the change in order of average particle size of the

GO nanosheets, suggesting that average particle size of GO nanosheets also influences the average pore size of the membranes. Further, at 2% GO-3/P membrane shows less number of uneven surface pores and smaller average pore size. This phenomenon could be because of poor dispersion of GO-3 in casting solution (Figure S3) and increased casting solution viscosity (Figure 4b). However, when the oxidation degree is increased further, 2% GO-5/P and 2% GO-7/P membranes show a sieve-like structure with an average pore size of 3.8 nm and 4.1 nm, respectively. The increased pore size of the membrane demonstrated the effect of increased hydrophilicity of GO-x at high oxidation level. In a comparison between different loadings of GO-5 at the same oxidation level, the porosity of the membrane surface initially increased to 2 wt% GO-5 content membrane and then decreased at 5 wt% GO-5 content membrane. This result can be explained by the fact that the loading of GO-5 in casting solution to 2 wt% increases the porosity of the membrane due to enhanced phase separation with hydrophilic GO-5. Further increase in GO-5 content to 5 wt% shows an increase in viscosity of casting solution that leads to forming a denser skin layer, resulting in a less porous structure due to delayed phase separation.

Bulk porosity (ε) of the membrane was determined using the procedure as mentioned in the experimental section and results are shown in Figure S4. The blending of GO-x in PSF casting solution enhanced the porosity of the membranes. The membrane porosity increased with increasing oxidation level in both 1% GO-x/P and 2% GO-x/P membranes. Increase in hydrophilicity of the GO-x at different oxidation levels enhances exchange of the solvent and the non-solvent during phase separation that gives highly porous membrane. At a different loading of GO-5 at the same oxidation level, the bulk porosity of membrane initially increases with GO-5 content to 2 wt% and then decreases at higher loading of 5 wt% GO-5. The decrease in bulk porosity of 5% GO-5/P membrane can be explained by the formation of a less porous structure, due to hindered phase separation associated with increased viscosity of casting solution.

The hydrophilicity of GO-x/P membrane was evaluated by measuring the water contact angle using the sessile drop method. In mixed matrix membranes, hydrophilicity of membrane is influenced by the hydrophilicity of the heterogeneous matrix. Loading and oxidation degree of GO-x influence the hydrophilicity and surface characteristics of resultant GO-x/P membranes. Membrane-water contact angle decreased with the decrease in the zeta potential of the suspension of GO-x nanosheets in water (Figure 6a). GO-x shows higher hydrophilic character with the increase in the degree of oxidation. Blending of GO-x in the PSF matrix increases the hydrophilicity of the membrane. The water contact angle values of all GO-x/P membrane are shown in Table 1. 10% PEG membrane without any GO-x addition shows the water contact angle of 67.9°. The blending of GO-x in PSF membrane decreased the water contact angle to 56°. Water contact angle of 1% GO-x/P membranes decreases to 61.8°, 59.7°, 58.2° for GO-3, GO-5, and GO-7 respectively. Increase in oxidation degree of GO-x increases the affinity towards water that helps it to migrate towards membrane/water interface quickly in order to minimize the interface energy during phase separation, enhancing hydrophilicity. Further, the increase in GO-x loading in PSF membrane to 2 wt% shows a decrease in water contact angle, except for 2% GO-3/P membrane. Upon comparing changes in water contact angle for differing amount of GO-5 in the matrix, the contact angle was found to reduce to 59.7° and 58.0° for 1 wt% and 2 wt%, respectively. Whereas, a slight increase in the water contact angle of the membrane to 60.7° was observed at 5 wt% loading of GO-5. Increase in solution viscosity may have affected the migration of hydrophilic GO-x nanosheets to the surface during phase inversion, causing an increase in the contact angle at higher GO-x loading. Thus, an increase in hydrophilic nature of GO-x decreases the membrane water contact angle and leads to form a porous membrane that results in higher permeability.

Zeta potential of the membrane (ζ) enables to understand the change in the chemistry of the membrane surface and the fouling tendency of the membrane after the blending of additives. GO-x/P membrane surface zeta potential was determined by measuring the streaming potential using the electro-kinetic

analyzer. Isoelectric point (pH value where no charge is present at the surface) was used to define the changes in membrane surface charge due to the blending of GO-x. The surface zeta potential of the GO-x/P membranes as a function of pH value is shown Figure 6b. 10 wt% PEG membrane showed an isoelectric point of 3.7. The membrane was positively charged at low pH and negatively charged at neutral and high pH. The blending of GO-x in polysulfone matrix caused a negative shift in the surface zeta potential curve, decreasing the isoelectric point of the membrane surface. For the 1% GO-x/P membrane, isoelectric point decreased to a pH of 3.5 for GO-3 and 3.4 for GO-5 content membrane respectively. However, 1% GO-7/P membrane was entirely negative charged over the pH range studied with no isoelectric point indicating a highly negatively charged surface. This behavior can be explained based on presence of highest oxygen functionalities on GO-7 surface, which also showed lowest zeta potential among the GO-x studied.

The mechanical properties of GO-x/P membrane were measured, and the result is shown in Table 1. The blending of GO-x to the PSF matrix increases the tensile strength of the membrane. The maximum load for 10% PEG membrane was 3.3 N. The 1% GO-x/P membrane showed a maximum load of 3.5 N, 3.8 N, and 3.9 N for GO-3, GO-5, and GO-7 content membrane, respectively. The blending of GO nanosheets in PSF membrane boosted the tensile strength due to the interaction of PSF matrix to GO [20]. Increased in oxidation level assisted dispersion of GO-x in casting solution that results in higher mechanical strength. Further, an increase in GO-x loading to 2 wt% in PSF membrane showed an increase in mechanical strength, except that GO-3 content membrane. The decrease in mechanical strength at 2% GO-3/P membrane is possibly due to the agglomeration and poor dispersion of GO-3 nanosheets in casting solution at lower oxidation degree. GO-5 content membrane showed an increase in mechanical strength first with increasing GO nanosheets loading to 2 wt% and further get constant at 5 wt% loading. Previous studies also found that the mechanical strength is increased by blending of GO nanosheets in PSF membrane [20,38].

3.3 Permeability performance and rejection studies of mixed matrix membranes

Membrane performance and rejection studies of the membrane were carried by the measurement of pure water permeability, BSA rejection, flux recovery on flushing fouled membrane with water. Table 1 gives the variation of membrane performance of GO-x/P membranes with GO-x as well as varying loading of GO-x in dope solution. All GO-x/P membranes showed higher water permeability compared to control 10% PEG membrane. Control membrane without any GO-x showed the lowest water permeability of 102.7 kg/m^2 h bar. The blending of GO-x in casting solution increased water permeability of the resultant membrane. The water permeability of 1% GO-3/P membrane was 215.7 kg/m^2 h bar, over 2-fold higher flux in comparison to the water permeability of the control 10% PEG membrane. The 1% GO-5/P membrane showed a decrease in water permeability to 207.2 kg/m^2 h bar with an increase of oxidation level in GO-5. However, further increase in the oxidation level in GO-7 resulted in an increase in water permeability of 1% GO-7/P membrane to 249.5 kg/m^2 h bar. The minima in water permeability value at 1% GO-5/P membrane can be explained by the smaller average particle size of GO-5 than GO-3 and GO-7. This result indicates that the water permeability of 1% GO-x/P membrane is dependent on both average particle size and oxidation degree of GO-x nanosheets, results in higher permeability. An increase of GO-x loading in 2% GO-x/P membrane showed further enhancement in water permeability with increasing oxidation degree of GO-x, except in 2% GO-3/P membrane. The 2% GO-7/P membrane exhibits the highest water permeability to 352.2 kg/m^2 h bar, which is 2.5-fold higher compared to control 10% PEG membrane. The decrease in water permeability of 2% GO-3/P membrane was supported by an increase in viscosity of the casting solution and lower hydrophilicity of GO-3.

GO-5 was selected for studying the effect of different loading of GO-x, due to the lowest particle size and highest BSA rejection. The water permeability of GO-5 content membrane was increased with

loading and reach maxima (255.5 kg/m^2 h bar) in 2% GO-5/P membrane. Further increase in loading of GO-5, the water permeability of 5% GO-5/P membrane decreases to 139.3 kg/m^2 h bar. An increase in concentration of GO-5 causes change in phase inversion due to two factors: (a) rising hydrophilicity of the matrix and (b) rising viscosity of the dope solution. An increase in the hydrophilicity enhances phase separation giving larger pore size, numerous pores and higher water permeability, while an increase in viscosity of dope solution hiders phase separation giving a smaller pore size with less number of pores. This behavior is seen when the GO-5 content of the membrane was 2 wt%, the hydrophilicity of nanosheets enhanced the phase separation that resulted in numerous pores and higher water permeability. Whereas at 5 wt% of GO-5 content of the membrane, the viscosity of the casting solution increased, which hindered the phase separation that gave a smaller pore size and lower water permeability.

Further, Figure 7a shows a comparison of water permeability of the membranes against the water contact angle for the membranes prepared. The control 10% PEG membrane had the highest contact angle and showed the lowest water permeability. The blending of GO-x in PSF membrane showed a decrease in contact angle and higher water permeability. Among GO-x/P membrane with different GO-x loading, membranes with GO-7 showed the lowest contact angle and highest water permeability for loading of both 1 wt% and 2 wt% in the dope solution. 2% GO-7/P membrane has the lowest contact angle of 56.0°, corresponding to the highest water permeability of 352.2 kg/m^2 h bar. The increase in permeability of GO-x/P mixed matrix membranes is mainly because of an increase in hydrophilicity (contact angle) and porosity. The hydrophilicity, chemical, and structural interactions of GO nanosheets with PEG and PSF in NMP are responsible for improving the performance of mixed matrix membrane [20]. Increase in oxygen-functional groups and smaller particle size of GO nanosheets show uniform dispersion in a polymer matrix that leads to the formation of many smaller pores in membrane leading to both higher permeability as well as higher rejection.

Rejection studies of the GO-x/P membranes were performed by filtration of 1000 mg/L BSA solution, and results are shown in Table 1. 10% PEG membrane without any GO-x shows BSA rejection of 91%. The blending of 1 wt% GO-x in PSF matrix shows an improvement in % BSA rejection of the mixed matrix membranes. The rejection of the membrane is first increasing with increase the oxidation degree of GO nanosheets to a threshold (93.0% for 1% GO-3/P and 98.9% for 1% GO-5/P) and then slightly decreased (97.2% for 1% GO-7/P). Similar rejection trend with lower value was observed with the 2% GO-x/P membranes prepared at 2 wt% loading of GO-x. The initial increase in BSA rejection with increasing the oxidation degree can be explained by the formation of many small pores and negatively charged membrane surface (Figure 6b.) Subsequently, at the highest oxidation degree of GO-7, BSA rejection is slightly decreased possibly due to the passage of BSA molecules through the larger pores of the membrane. Whereas, at a different loading of GO-5 at same oxidation degree in membrane show decrease in % BSA rejection with an increasing amount of GO-5 to 2 wt%, then slightly increases at the highest loading of 5 wt%. This behavior of the % BSA rejection of the membrane is due to an initial increase in porosity for lower loading and then a decrease at higher loading of GO-5 (Figure 5 and Figure S4). Further, a comparison plot of % BSA rejection of the membranes against water permeability of that membrane is shown in Figure 7b. The membrane with both high water permeability and high % BSA rejection is desired. 10% PEG membrane has the lowest water permeability with lower BSA rejection. In 1 wt% GO-x/P and 2 wt% GO-x/P membranes, GO-5 content membrane showed the maxima in % BSA rejection with intermediate water permeability; whereas GO-7 content membrane showed a decrease in % BSA rejection with highest water permeability. 1% GO-7/P membrane has a higher % BSA rejection compared to 2% GO-5/P membrane at almost the same water permeability showing that the effect of higher oxidation level in GO-7. Thus, GO-7 with higher oxidation degree gave a high-throughput membrane at lower loading (1 wt%). At higher loading of GO-7 (2 wt%) in the membrane, highest permeability membrane was obtained with marginal reduction with BSA rejection.

3.4 Antifouling performance of mixed matrix membranes

The performance of the aqueous membrane filtration considerably depends upon the fouling potential of the membrane. An efficient membrane should possess a higher permeability, higher rejection, and low fouling tendency for long-term use. Membrane fouling potential mainly depends upon hydrophilicity of the membrane. The blending of GO nanosheets in polymer matrix proved the practical and convenient approach for enhancement in permeability and fouling resistance properties of the membrane [17]. Antifouling performance of GO-x/P membrane was performed by measuring the recovered water permeability (P_w^f) after the membrane was fouled by 1000 mg/L BSA solution. Figure 8a shows the permeability of the membrane at different filtration stages (DI water – BSA solution – DI water) as a function of time. Water permeability of the fouled membrane was measured after simple water wash of membrane in the filtration cell itself for 10 min. Overall, the permeability of membrane during 1000 mg/L BSA filtration (P_{BSA}) was decreased compared to that DI water permeability (P_w^i) that represents the fouling of the membrane. Recovered water permeability (P_w^f) of the fouled 10% PEG/P membrane after water washing showed a significant decrease in value in comparison to the initial water permeability (P_w^i). However, the blending of GO-x in casting solution showed an increase in recovered water permeability (P_w^f) of mixed matrix membranes with an increase in oxidation level.

Membrane surface charge plays an important role in rejecting BSA protein molecules via electrostatic interactions during the filtration that helps us to understand the membrane fouling tendency. Membrane surface zeta potential (ζ) at pH 7.4 (same pH during BSA filtration) was analyzed by measuring the streaming potential using the electro-kinetic analyzer. A plot of permeability recovery ratio ($\%\ P_{rec}$) against the membrane surface zeta potential (ζ) at pH 7.4 is plotted in Figure 8b. This plot will help to understand the relation between the hydrophilicity of the membrane surface and the

antifouling property. Membrane surface with lower zeta potential value showed higher permeability recovery ratio ($\% P_{rec}$). 10% PEG membrane without any GO-x with the highest surface zeta potential exhibited poor permeability recovery ratio after BSA fouling signifying its high fouling potential. Blending of 1 wt% GO-x in polysulfone membrane showed an increase in permeability recovery ratio at lower surface zeta potential with an increase in oxidation degree. Approximately, 84.5%, 95.4%, and 99.0% of the water permeability were recovered after simple water flushing of 1% GO-3/P, 1% GO-5/P, and 1% GO-7/P membrane, respectively. Increase in GO-x loading at 2 wt%, similar $\% P_{rec}$ was observed for 2% GO-3/P (84.7%) and 2% GO-5/P (94.2%) membrane, except reduction in $\% P_{rec}$ to 71.9% of 2% GO-7/P membrane. The reduction in $\% P_{rec}$ of 2% GO-7/P membrane possibly due to protein deposition in larger pores of the membrane. Further, at higher loading of GO-5 in casting solution lead to an increase in surface zeta potential as well a slight decrease in permeability recovery ratio of the membrane. The decrease in $\% P_{rec}$ at 5 wt% loading of GO-5, due to adsorption of protein molecules in large pores/defects and lower electrostatic repulsion between protein molecules and membrane surface. Reversible fouling ratio ($\% R_r$) and irreversible fouling ratio ($\% R_{ir}$) for fabricated mixed matrix membranes were calculated to get insight into membrane fouling type, and are shown in Figure 8c. 10% PEG membrane without any GO-x shows highest irreversible fouling ratio of 31.5%, displays extreme fouling potential. In 1% GO-x/P membrane, the irreversible fouling ratio decreased with an increase in oxidation degree of GO, and it reached a minima value to 1% of GO-7 content membrane. In 2% GO-x/P membrane, irreversible fouling ratio is decreased further in GO-3 and GO-5 content membrane. Whereas, 2% GO-7/P membrane shows increased in the irreversible fouling ratio, perhaps due to protein deposition in large-sized pores. Blending of different loading of GO-5 from 1 wt% to 5 wt% in casting solution showed a slight increase in irreversible fouling ratio of the membranes. All GO-x/P membranes demonstrate higher reversible fouling ratio compared to that control 10% PEG membrane. Higher reversible fouling in GO-x/P membranes caused by deposition of protein molecules on the

membrane surface, which is further washed out using simple water flushing result in higher permeability recovery ratio ($\% P_{rec}$). Overall, the results indicate that antifouling property of the membrane is enhanced by blending of GO-x. The highest water permeability recovery ratio reached to 99.0% for 1% GO-7/P membrane, which follows the trend of lower membrane surface zeta potential.

The performance of GO-x/P membrane is compared with the other state-of-art carbon-based, and inorganic additives content polymer mixed matrix membrane (Figure 9). The GO-x/P mixed matrix membrane showed higher water permeability as well as higher antifouling potential against BSA, compared to other mixed matrix membranes. Furthermore, an increase in oxidation degree of GO modifies the microstructure and improves the performance of polysulfone mixed matrix membrane that is much higher than previously reported the different degree of reduced GO content mixed matrix membrane [39]. Thus, the different oxidation degree GO is a promising additive in polysulfone to fabricate varying pore size mixed matrix membrane having high permeability and high rejection.

4 Conclusions

We found that increasing the degree of oxidation decreased the C/O ratio in GO as expected. The proportion of carbonyl and carboxyl groups in the matrix also increased, lowering the zeta potential, and increasing dispersibility in water, NMP as well as casting solution. Uniform dispersion of GO-x in PSF casting solution enhanced the phase inversion characteristics resulting in well-defined membrane microstructure and interconnected transport channels. The presence of GO-x in the membrane narrowed pore size distribution and improved porosity and tensile strength. Hydrophilic GO-x decreased the water contact angle of the membranes, lowered the hydraulic resistance to water transport, and yielded lower irreversible fouling. As the loading of GO-x increased, the porosity increased, and the pore structure became more open, giving a slightly lower permeability recovery ratio than the optimal GO-x

loading of 1 %, possibly due to the protein deposition within the pores. The irreversible fouling decreased with increasing oxidation degree of the external matrix, GO. The membrane contains GO-7 having the highest oxidation degree gave permanent negative charge to membrane for all pH. This membrane exhibited exceptional resistance to BSA fouling giving 99 % flux recovery on simple water flushing. The flux of this membrane was about 2.5 times that of the control membrane, with about 97% rejection, which was substantially better than the control membrane. The flux rejection trade-off in the membranes is transcended by the addition of GO-x to the membrane. Water, the anti-solvent exhibits high mobility in the matrix, which gives rise to thermodynamic instabilities, causing phase inversion giving unique membrane microstructure with suppressed finger-like porous geometry. Increased oxidation of GO-x enhances this effect. While the particle size and the nature of the matrix is similar, the effects in the membrane microstructure and the resulting performance are attributed to the enhanced oxygen %, causing enhanced hydrophilicity and high mobility to water within the matrix. It also explains the enhanced properties of membranes with microporous hydrophilic matrices like zeolites over other relatively nonporous particles. In conclusion, the properties of the membranes can be tuned using microporous hydrophilic matrices like graphene oxide that can facilitate internal diffusion of anti-solvent developing membrane microstructure for high performance.

5 Acknowledgments

The authors are thankful to the University Grants Commission of India for support under UGC-Special Assistant Program and UGC-Faculty Research Promotion Scheme. The authors would also like to thank the Department of Science and Technology for support under the Fund for Improvement of S&T infrastructure in universities & higher educational institutions. Authors would like to acknowledge the Environment and Water Technology Centre of Innovation, Ngee Ann Polytechnic, Singapore for

assistance with scanning electron microscopy and tensile strength measurements, Sophisticated Analytical Instrumentation Facility at Indian Institute of Technology Bombay for assistance with elemental analysis, National Centre for Nanosciences and Nanotechnology, University of Mumbai for assistance with X-ray photoelectron microscopy.

6 References

[1] S. Adham, A. Hussain, J. Minier-Matar, A. Janson, R. Sharma, Membrane applications and opportunities for water management in the oil & gas industry, Desalination. 440 (2018) 2–17. https://doi.org/10.1016/j.desal.2018.01.030.

[2] J. Wang, A. Cahyadi, B. Wu, W. Pee, A.G. Fane, J.W. Chew, The roles of particles in enhancing membrane filtration: A review, Journal of Membrane Science. 595 (2020) 117570. https://doi.org/10.1016/j.memsci.2019.117570.

[3] M.F.A. Goosen, S.S. Sablani, H. Al-Hinai, S. Al-Obeidani, R. Al-Belushi, D. Jackson, Fouling of Reverse Osmosis and Ultrafiltration Membranes: A Critical Review, Separation Science and Technology. 39 (2005) 2261–2297. https://doi.org/10.1081/SS-120039343.

[4] X. Shi, G. Tal, N.P. Hankins, V. Gitis, Fouling and cleaning of ultrafiltration membranes: A review, Journal of Water Process Engineering. 1 (2014) 121–138. https://doi.org/10.1016/j.jwpe.2014.04.003.

[5] S. Kim, K.H. Chu, Y.A.J. Al-Hamadani, C.M. Park, M. Jang, D.-H. Kim, M. Yu, J. Heo, Y. Yoon, Removal of contaminants of emerging concern by membranes in water and wastewater: A review, Chemical Engineering Journal. 335 (2018) 896–914. https://doi.org/10.1016/j.cej.2017.11.044.

[6] S. Al-Amshawee, M.Y.B.M. Yunus, A.A.M. Azoddein, D.G. Hassell, I.H. Dakhil, H.A. Hasan, Electrodialysis desalination for water and wastewater: A review, Chemical Engineering Journal. 380 (2020) 122231. https://doi.org/10.1016/j.cej.2019.122231.

[7] M. Vinoba, M. Bhagiyalakshmi, Y. Alqaheem, A.A. Alomair, A. Pérez, M.S. Rana, Recent progress of fillers in mixed matrix membranes for CO2 separation: A review, Separation and Purification Technology. 188 (2017) 431–450. https://doi.org/10.1016/j.seppur.2017.07.051.

[8] H. Vinh-Thang, S. Kaliaguine, Predictive Models for Mixed-Matrix Membrane Performance: A Review, Chem. Rev. 113 (2013) 4980–5028. https://doi.org/10.1021/cr3003888.

[9] Y. Cheng, Y. Ying, S. Japip, S.-D. Jiang, T.-S. Chung, S. Zhang, D. Zhao, Advanced Porous Materials in Mixed Matrix Membranes, Advanced Materials. 30 (2018) 1802401. https://doi.org/10.1002/adma.201802401.

[10] R.D. Noble, Perspectives on mixed matrix membranes, Journal of Membrane Science. 378 (2011) 393–397. https://doi.org/10.1016/j.memsci.2011.05.031.

[11] J. Dechnik, C.J. Sumby, C. Janiak, Enhancing Mixed-Matrix Membrane Performance with Metal–Organic Framework Additives, Crystal Growth & Design. 17 (2017) 4467–4488. https://doi.org/10.1021/acs.cgd.7b00595.

[12] D. Qadir, H. Mukhtar, L.K. Keong, Mixed Matrix Membranes for Water Purification Applications, Separation & Purification Reviews. 46 (2017) 62–80. https://doi.org/10.1080/15422119.2016.1196460.

[13] J. Dechnik, J. Gascon, C.J. Doonan, C. Janiak, C.J. Sumby, Mixed-Matrix Membranes, Angewandte Chemie International Edition. 56 (2017) 9292–9310. https://doi.org/10.1002/anie.201701109.

[14] L. Yu, Y. Zhang, B. Zhang, J. Liu, H. Zhang, C. Song, Preparation and characterization of HPEI-GO/PES ultrafiltration membrane with antifouling and antibacterial properties, Journal of Membrane Science. 447 (2013) 452–462. https://doi.org/10.1016/j.memsci.2013.07.042.

[15] F. Perreault, A.F. de Faria, M. Elimelech, Environmental applications of graphene-based nanomaterials, Chem. Soc. Rev. 44 (2015) 5861–5896. https://doi.org/10.1039/C5CS00021A.

[16] D.R. Dreyer, S. Park, C.W. Bielawski, R.S. Ruoff, The chemistry of graphene oxide, Chem. Soc. Rev. 39 (2009) 228–240. https://doi.org/10.1039/B917103G.

[17] S. Zinadini, A.A. Zinatizadeh, M. Rahimi, V. Vatanpour, H. Zangeneh, Preparation of a novel antifouling mixed matrix PES membrane by embedding graphene oxide nanoplates, Journal of Membrane Science. 453 (2014) 292–301. https://doi.org/10.1016/j.memsci.2013.10.070.

[18] C.A. Crock, A.R. Rogensues, W. Shan, V.V. Tarabara, Polymer nanocomposites with graphene-based hierarchical fillers as materials for multifunctional water treatment membranes, Water Research. 47 (2013) 3984–3996. https://doi.org/10.1016/j.watres.2012.10.057.

[19] Z. Zhang, Q. An, Y. Ji, J. Qian, C. Gao, Effect of zero shear viscosity of the casting solution on the morphology and permeability of polysulfone membrane prepared via the phase-inversion process, Desalination. 260 (2010) 43–50. https://doi.org/10.1016/j.desal.2010.05.002.

[20] R.S. Zambare, K.B. Dhopte, A.V. Patwardhan, P.R. Nemade, Polyamine functionalized graphene oxide polysulfone mixed matrix membranes with improved hydrophilicity and anti-fouling properties, Desalination. 403 (2017) 24–35. https://doi.org/10.1016/j.desal.2016.02.003.

[21] J. Guerrero-Contreras, F. Caballero-Briones, Graphene oxide powders with different oxidation degree, prepared by synthesis variations of the Hummers method, Materials Chemistry and Physics. 153 (2015) 209–220. https://doi.org/10.1016/j.matchemphys.2015.01.005.

[22] B.M. Ganesh, A.M. Isloor, A.F. Ismail, Enhanced hydrophilicity and salt rejection study of graphene oxide-polysulfone mixed matrix membrane, Desalination. 313 (2013) 199–207. https://doi.org/10.1016/j.desal.2012.11.037.

[23] J. Lee, H.-R. Chae, Y.J. Won, K. Lee, C.-H. Lee, H.H. Lee, I.-C. Kim, J.-M. Lee, Graphene oxide nanoplatelets composite membrane with hydrophilic and antifouling properties for wastewater treatment, Journal of Membrane Science. 448 (2013) 223–230.

[24] K.B. Dhopte, R.S. Zambare, A.V. Patwardhan, P.R. Nemade, Role of Degree of Oxidation of Graphene Oxide on Biginelli Reaction Kinetics, ChemistrySelect. 2 (2017) 10997–11006. https://doi.org/10.1002/slct.201702064.

[25] K. Krishnamoorthy, M. Veerapandian, K. Yun, S.-J. Kim, The chemical and structural analysis of graphene oxide with different degrees of oxidation, Carbon. 53 (2013) 38–49. https://doi.org/10.1016/j.carbon.2012.10.013.

[26] G. Dong, J. Hou, J. Wang, Y. Zhang, V. Chen, J. Liu, Enhanced CO2/N2 separation by porous reduced graphene oxide/Pebax mixed matrix membranes, Journal of Membrane Science. 520 (2016) 860–868. https://doi.org/10.1016/j.memsci.2016.08.059.

[27] W.S. Hummers, R.E. Offeman, Preparation of Graphitic Oxide, J. Am. Chem. Soc. 80 (1958) 1339–1339. https://doi.org/10.1021/ja01539a017.

[28] K.B. Dhopte, R.S. Zambare, A.V. Patwardhan, P.R. Nemade, Role of graphene oxide as a heterogeneous acid catalyst and benign oxidant for synthesis of benzimidazoles and benzothiazoles, RSC Adv. 6 (2016) 8164–8172. https://doi.org/10.1039/C5RA19066E.

[29] L.G. Cançado, K. Takai, T. Enoki, M. Endo, Y.A. Kim, H. Mizusaki, A. Jorio, L.N. Coelho, R. Magalhães-Paniago, M.A. Pimenta, General equation for the determination of the crystallite size La of

nanographite by Raman spectroscopy, Appl. Phys. Lett. 88 (2006) 163106. https://doi.org/10.1063/1.2196057.

[30] C. Hontoria-Lucas, A.J. López-Peinado, J. de D. López-González, M.L. Rojas-Cervantes, R.M. Martín-Aranda, Study of oxygen-containing groups in a series of graphite oxides: Physical and chemical characterization, Carbon. 33 (1995) 1585–1592. https://doi.org/10.1016/0008-6223(95)00120-3.

[31] T. Wang, L. Zhao, J. Shen, L. Wu, B. Van der Bruggen, Enhanced Performance of Polyurethane Hybrid Membranes for CO2 Separation by Incorporating Graphene Oxide: The Relationship between Membrane Performance and Morphology of Graphene Oxide, Environ. Sci. Technol. 49 (2015) 8004–8011. https://doi.org/10.1021/acs.est.5b00138.

[32] M. Lotya, A. Rakovich, J.F. Donegan, J.N. Coleman, Measuring the lateral size of liquid-exfoliated nanosheets with dynamic light scattering, Nanotechnology. 24 (2013) 265703. https://doi.org/10.1088/0957-4484/24/26/265703.

[33] B.R. Coleman, T. Knight, V. Gies, Z.J. Jakubek, S. Zou, Manipulation and Quantification of Graphene Oxide Flake Size: Photoluminescence and Cytotoxicity, ACS Appl. Mater. Interfaces. 9 (2017) 28911–28921. https://doi.org/10.1021/acsami.7b08585.

[34] W.H. Walton, Feret‘s Statistical Diameter as a Measure of Particle Size, Nature. 162 (1948) 329–330. https://doi.org/10.1038/162329b0.

[35] G.D.J. Phillies, Translational diffusion coefficient of macroparticles in solvents of high viscosity, J. Phys. Chem. 85 (1981) 2838–2843. https://doi.org/10.1021/j150619a029.

[36] B. Gupta, N. Kumar, K. Panda, V. Kanan, S. Joshi, I. Visoly-Fisher, Role of oxygen functional groups in reduced graphene oxide for lubrication, Sci Rep. 7 (2017). https://doi.org/10.1038/srep45030.

[37] R.K. Layek, A.K. Nandi, A review on synthesis and properties of polymer functionalized graphene, Polymer. 54 (2013) 5087–5103. https://doi.org/10.1016/j.polymer.2013.06.027.

[38] M. Ionita, A.M. Pandele, L. Crica, L. Pilan, Improving the thermal and mechanical properties of polysulfone by incorporation of graphene oxide, Composites Part B: Engineering. 59 (2014) 133–139. https://doi.org/10.1016/j.compositesb.2013.11.018.

[39] N. Meng, R.C.E. Priestley, Y. Zhang, H. Wang, X. Zhang, The effect of reduction degree of GO nanosheets on microstructure and performance of PVDF/GO hybrid membranes, Journal of Membrane Science. 501 (2016) 169–178. https://doi.org/10.1016/j.memsci.2015.12.004.

List of tables

Table 1. Properties of the membranes[2].

Membrane	Casting solution viscosity[3] (Pa.s)	Contact angle (°)	Porosity (%)	Average pore size (nm)	Maximum load (N)	P_w^i (kg/m^2 h bar)	R_{BSA} (%)	Membrane zeta potential (ζ) at pH 7.4	% P_{rec}
10% PEG	0.33	67.9	25.1	2.7	3.3	102.7	91.0	-36.0	68.5
1% GO-3/P	0.33	61.8	34.1	3.9	3.5	215.7	93.0	-39.0	84.5
1% GO-5/P	0.34	59.7	36.4	3.2	3.8	207.2	98.9	-45.0	95.4
1% GO-7/P	0.28	58.2	36.4	3.7	3.9	249.5	97.2	-48.2	99.0
2% GO-3/P	0.37	62.7	38.4	3.2	3.5	109.5	87.9	-36.5	84.7
2% GO-5/P	0.36	58.0	39.9	3.8	4.2	255.5	90.2	-40.6	94.2
2% GO-7/P	0.30	56.0	42.5	4.1	4.3	352.2	88.6	-43.9	71.9
5% GO-5/P	0.77	60.7	29.4	2.7	4.2	139.3	96.1	-38.0	91.2

[2] GO-1 not considered for studies due to formation of big pores and lowest BSA rejection.

[3] Casting solution viscosity at 10 s^{-1} shear rate.

List of figures

Inset shows change in IEP of the membrane due to the addition of GO with different degree of oxidation.

Figure 7. (a) Change in water permeability with the contact angle of the synthesized mixed matrix membranes; (b) Comparison of % BSA rejection versus water permeability of the membranes.

Figure 8. (a) Permeability of 1% GO-x/P membrane as a function of filtration time. (b) Permeability recovery ratio ($\% \, \mathrm{Prec}$) versus membrane surface zeta potential (ζ) at membrane at pH 7.4. (c) Fouling resistance ratio of GO-x/P mixed matrix membranes.xx

Figure 9. Performance comparison of state-of-art mixed matrix membrane for various additives.

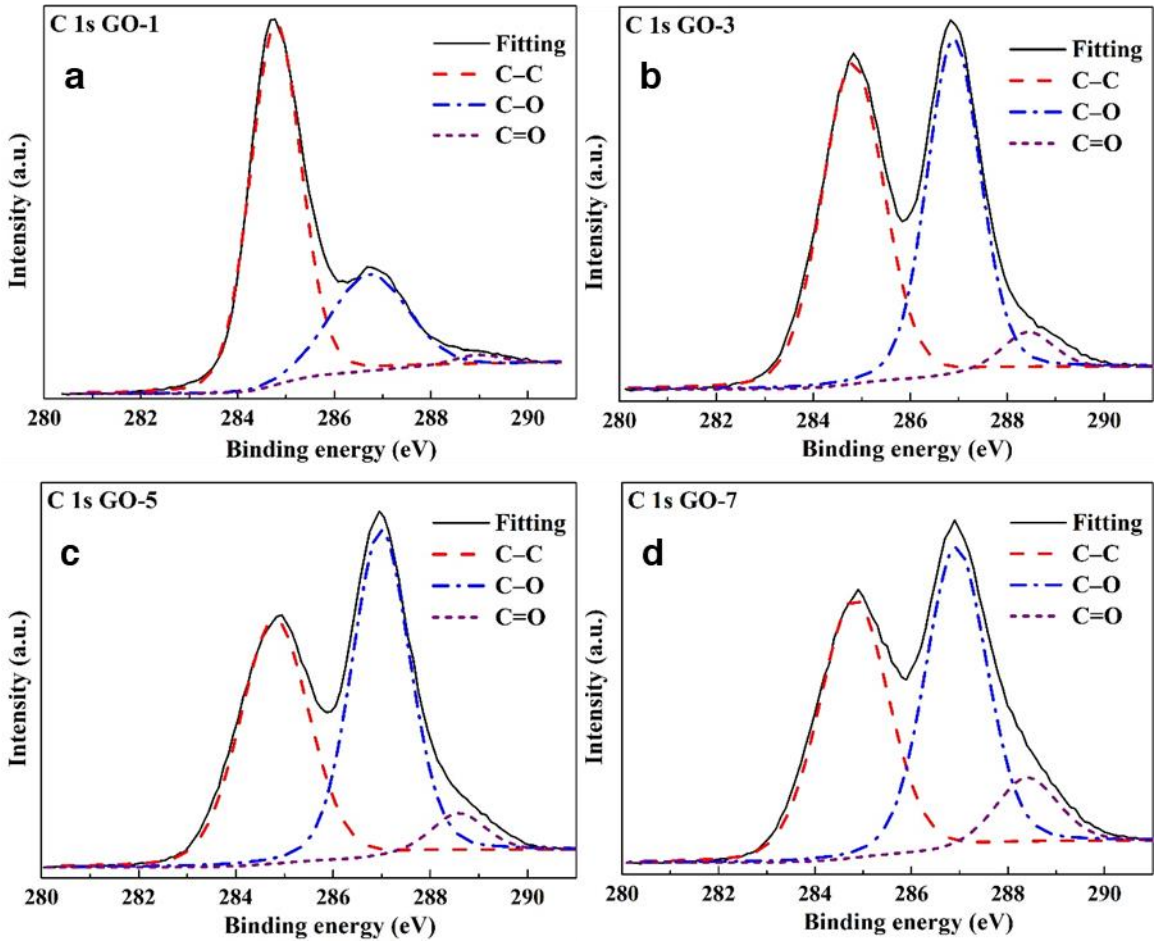

Figure 1. High-resolution XPS C 1s spectra of (a) GO-1; (b) GO-3; (c) GO-5 and (d) GO-7.

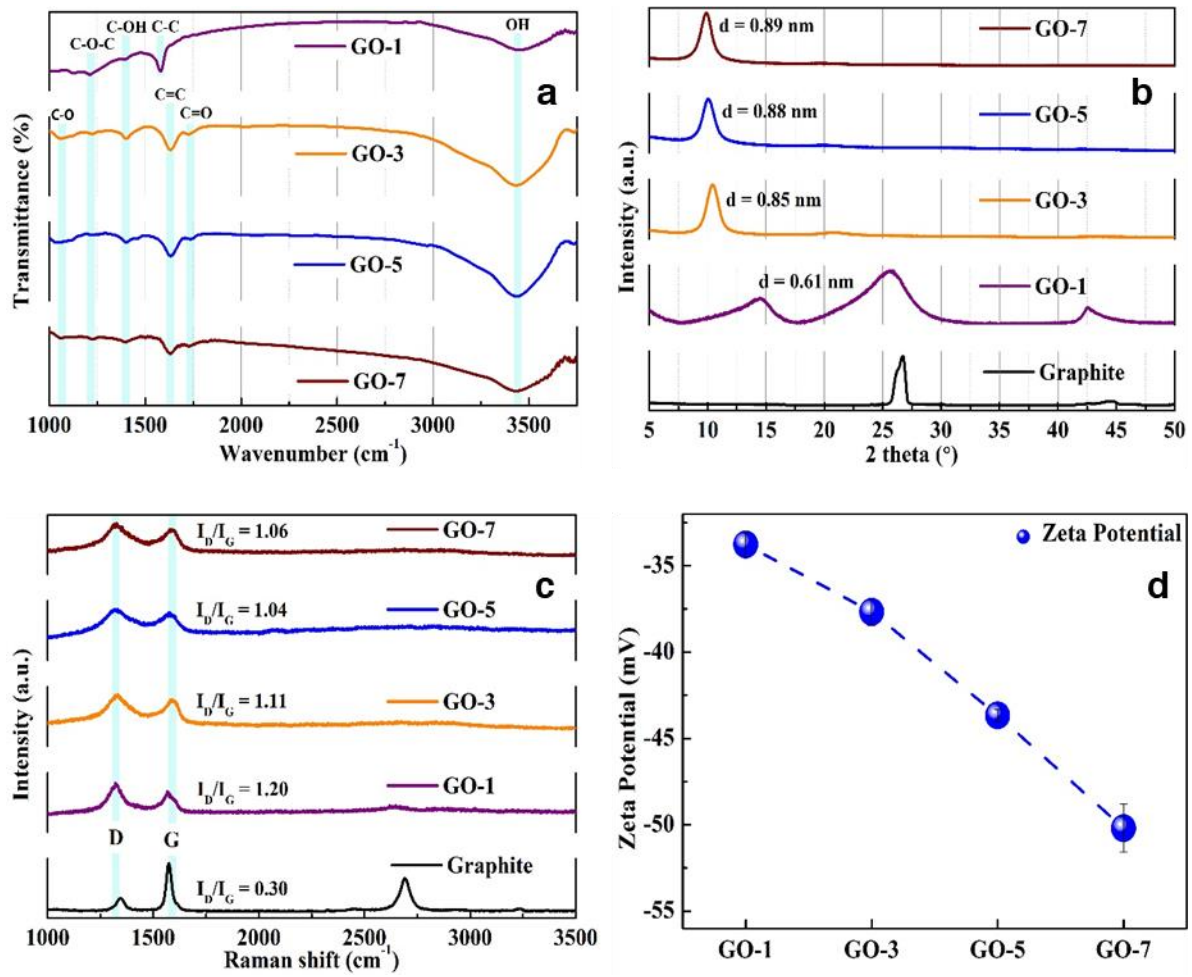

Figure 2. (a) FT-IR spectra of GO-x; (b) XRD spectra of GO-x; (c) Raman analysis of GO-x; (d) Variation in the zeta potential of GO with different oxidation degree.

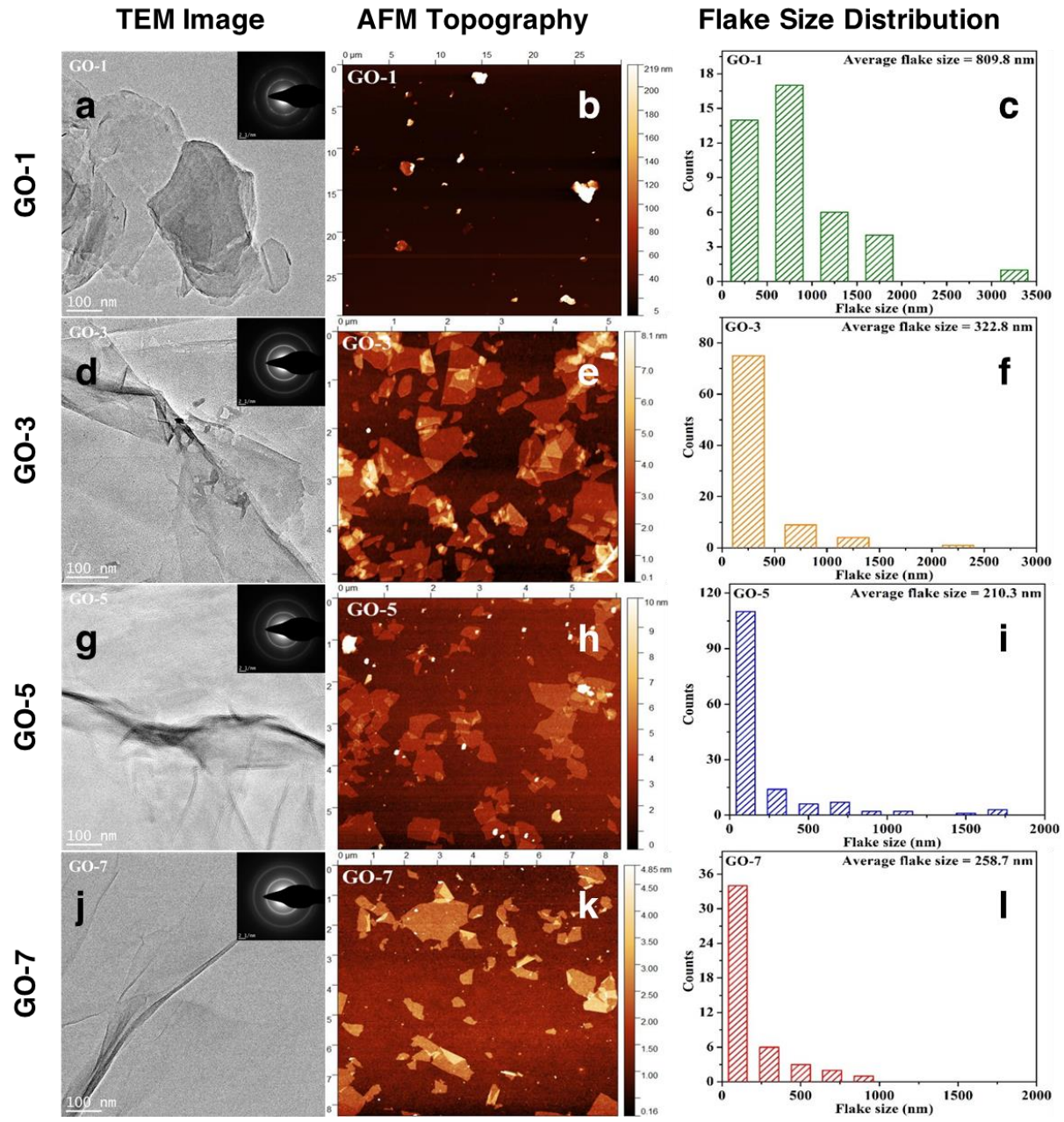

Figure 3. TEM, AFM topography and size distribution of GO-x flakes estimated from AFM image of GO-x. TEM images of (a) GO-1; (d) GO-3; (g) GO-5; (j) GO-7; AFM topography of (b) GO-1, (e) GO-3; (h) GO-5; (k) GO-7; Flake size distribution of (c) GO-1; (f) GO-3; (i) GO-5; (l) GO-7.

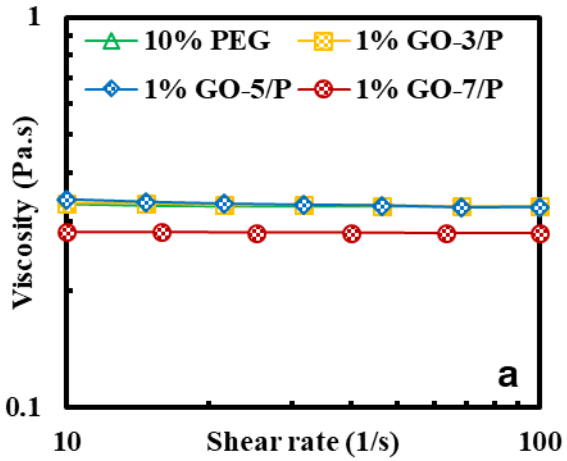
1
10% PEG
1% GO-3/P
1% GO-5/P
1% GO-7/P
Viscosity (Pa.s)
a
0.1
10
Shear rate (1/s)
100

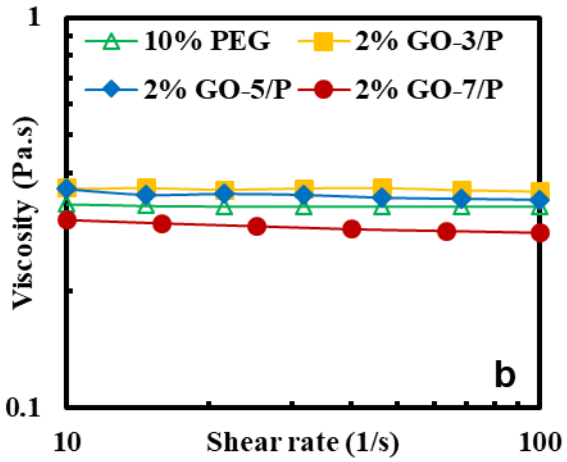
1
10% PEG
2% GO-3/P
2% GO-5/P
2% GO-7/P
Viscosity (Pa.s)
b
0.1
10
Shear rate (1/s)
100

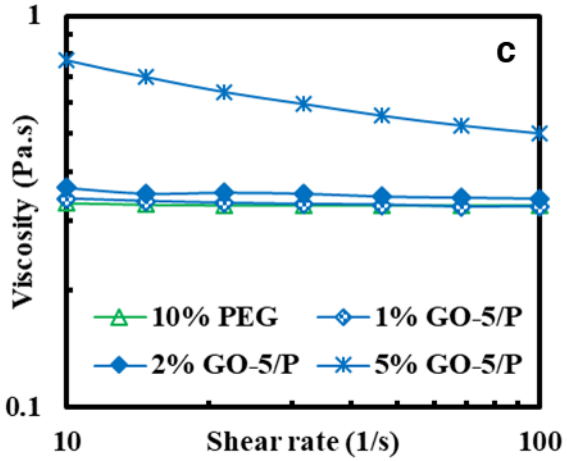
1
c
Viscosity (Pa.s)
10% PEG
1% GO-5/P
2% GO-5/P
5% GO-5/P
0.1
10
Shear rate (1/s)
100

Figure 4. Variation in viscosity of membrane dope solution with shear rate[4]. (a) 1% GO-x/P; (b) 2% GO-x/P; (c) Different loading of GO-5.

[4] GO-1 not considered for studies due to the formation of big pores and lowest BSA rejection.

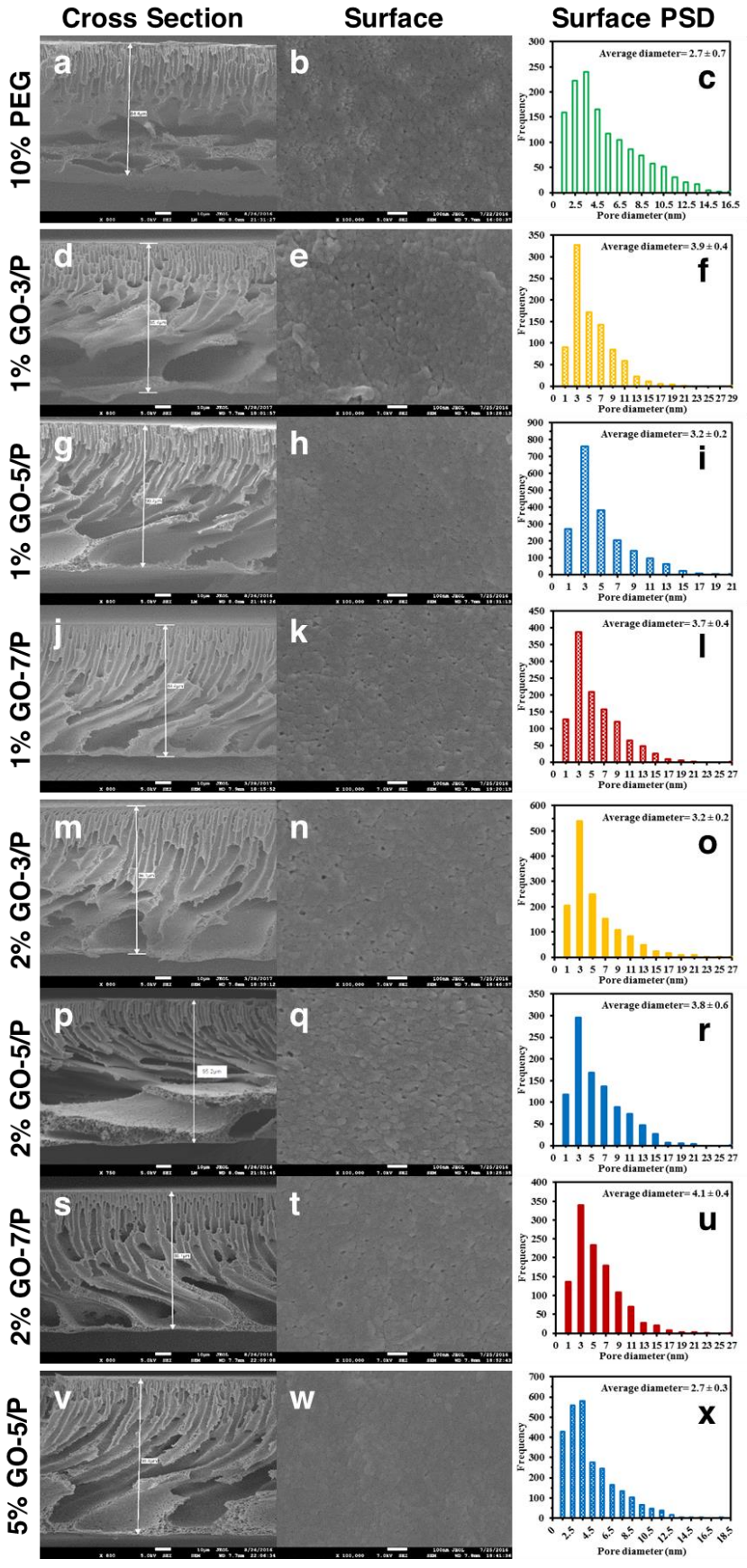
Cross Section
Surface
Surface PSD
10% PEG
1% GO-3/P
1% GO-5/P
1% GO-7/P
2% GO-3/P
2% GO-5/P
2% GO-7/P
5% GO-5/P
a
b
c
d
e
f
g
h
i
j
k
l
m
n
o
p
q
r
s
t
u
v
w
Average diameter= 2.7 ± 0.7
Average diameter= 3.9 ± 0.4
Average diameter= 3.2 ± 0.2
Average diameter= 3.7 ± 0.4
Average diameter= 3.2 ± 0.2
Average diameter= 3.8 ± 0.6
Average diameter= 4.1 ± 0.4
Average diameter= 2.7 ± 0.3
Frequency
Pore diameter (nm)

Figure 5. SEM images of cross section and surface, and surface pore size distribution (PSD) estimated from image analysis of SEM images of surface of membranes synthesized. Cross section images of (a) 10 % PEG membrane; (d) 1 % GO-3/P membrane; (g) 1 % GO-5/P membrane; (j) 1 % GO-7/P membrane; (m) 2 % GO-3/P membrane; (p) 2 % GO-5/P membrane; (s) 2 % GO-7/P membrane; (v) 5 % GO-5/P membrane. SEM image of surface of (b) 10 % PEG membrane; (e) 1 % GO-3/P membrane; (h) 1 % GO-5/P membrane; (k) 1 % GO-7/P membrane; (n) 2 % GO-3/P membrane; (q) 2 % GO-5/P membrane; (t) 2 % GO-7/P membrane; (w) 5 % GO-5/P membrane. Surface pore size distribution estimated from SEM of surface of (c) 10 % PEG membrane; (f) 1 % GO-3/P membrane; (i) 1 % GO-5/P membrane; (l) 1 % GO-7/P membrane; (o) 2 % GO-3/P membrane; (r) 2 % GO-5/P membrane; (u) 2 % GO-7/P membrane; (x) 5 % GO-5/P membrane;

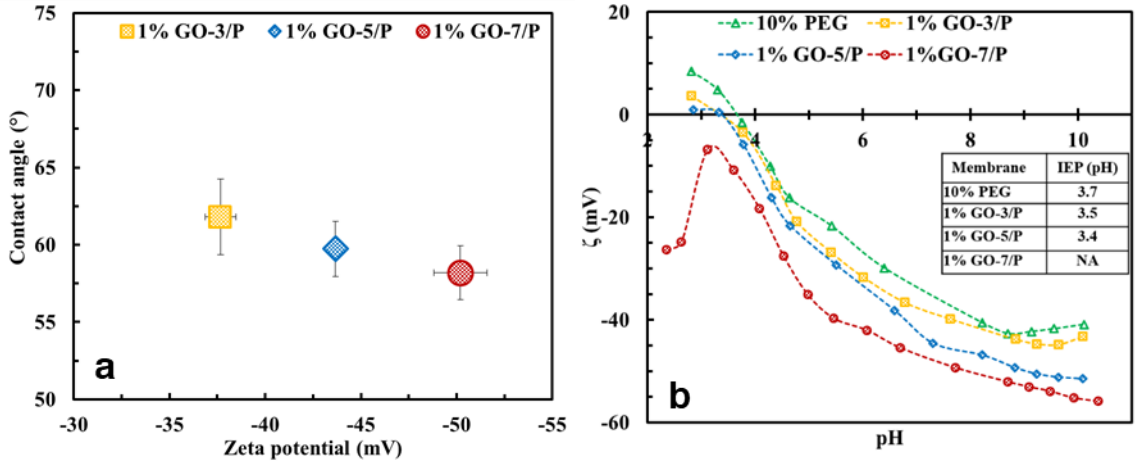

Figure 6. (a) Variation of contact angle of the membranes with a zeta potential of 100 mg/L dispersion of GO-x in water; (b) Variation in surface charge (ζ) of 1% GO-x/P membrane as a function of pH value. Inset shows change in IEP of the membrane due to the addition of GO with different degree of oxidation.

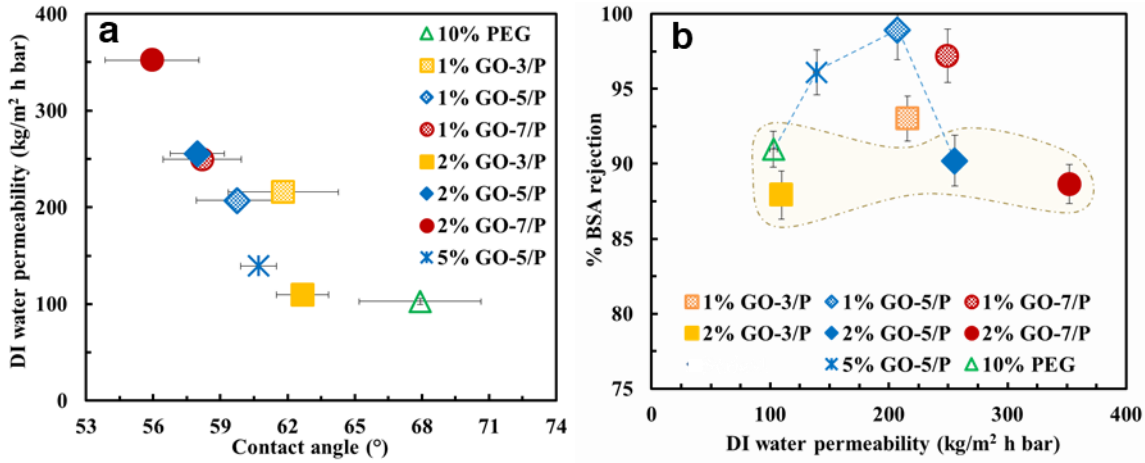

Figure 7. (a) Change in water permeability with the contact angle of the synthesized mixed matrix membranes; (b) Comparison of % BSA rejection versus water permeability of the membranes.

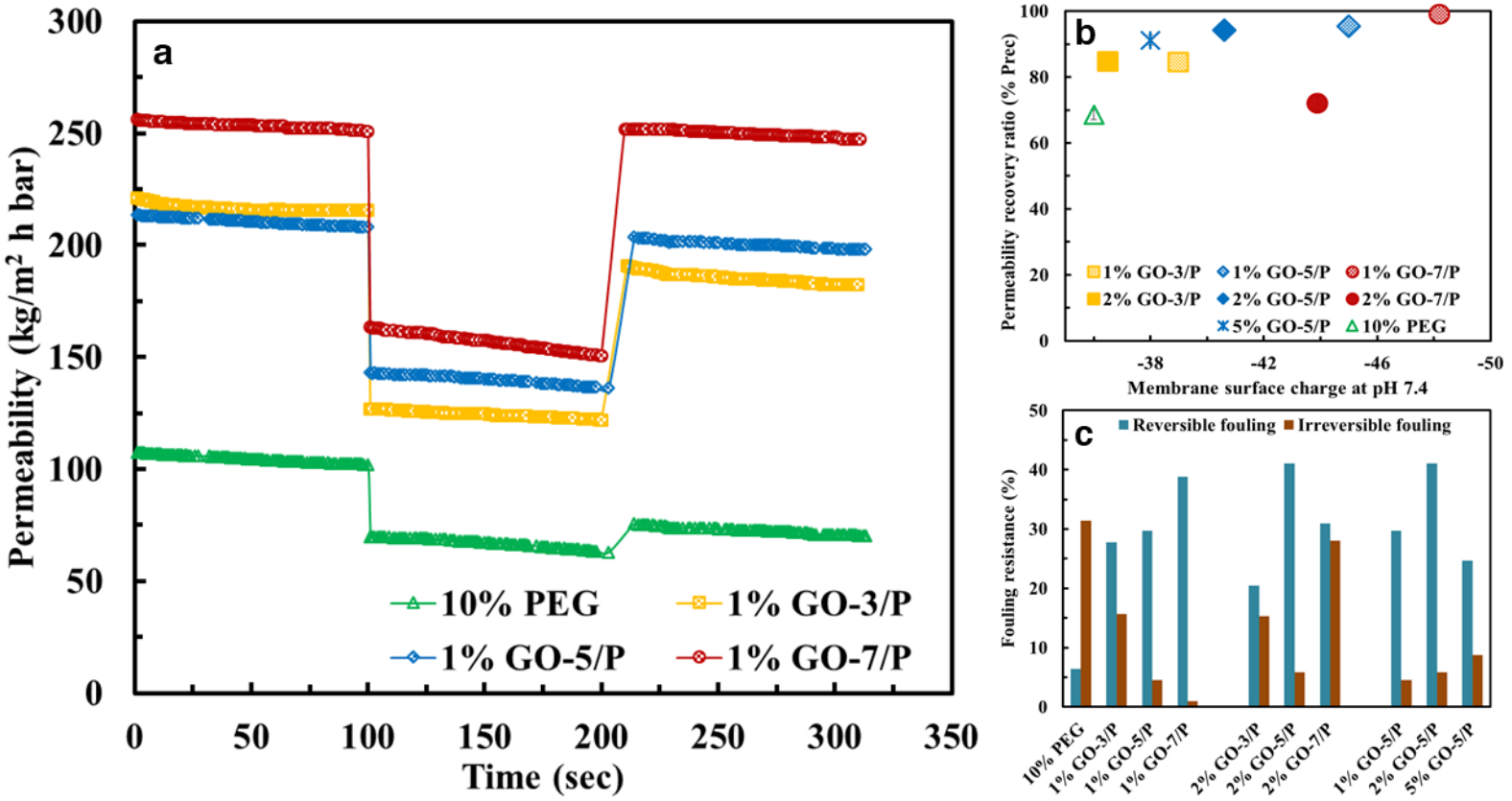

Figure 8. (a) Permeability of 1% GO-x/P membrane as a function of filtration time. (b) Permeability recovery ratio (% P_{rec}) versus membrane surface zeta potential (ζ) at membrane at pH 7.4. (c) Fouling resistance ratio of GO-x/P mixed matrix membranes.xx

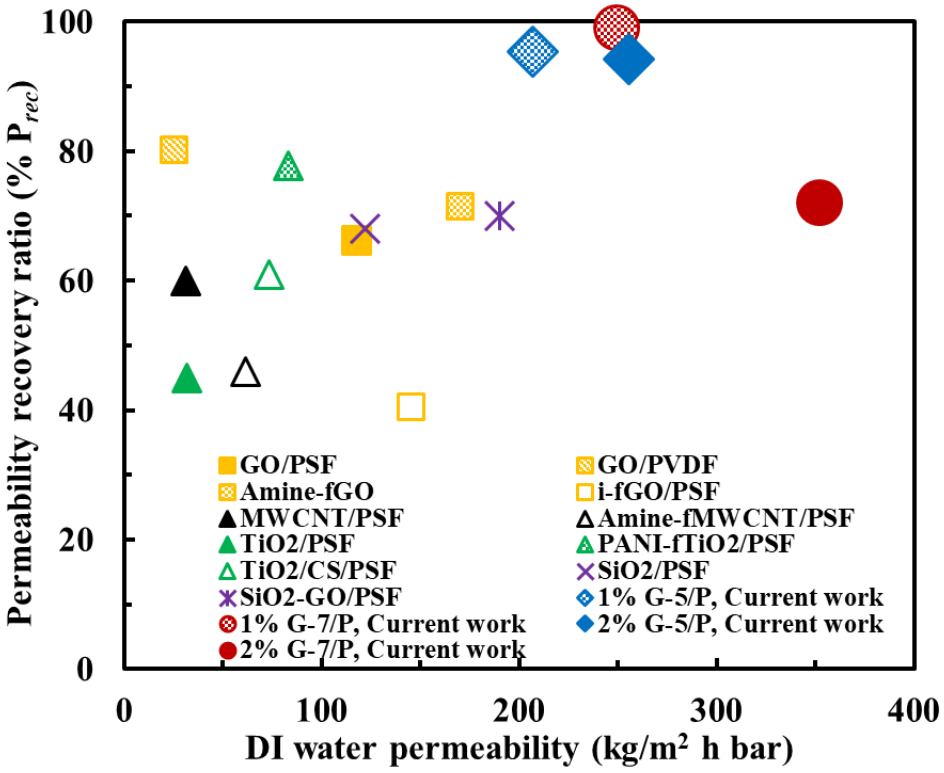

Figure 9. Performance comparison of state-of-art mixed matrix membrane for various additives.

RSZ: Conceptualization, Methodology, Investigation, Writing-Original Draft

KBD: Methodology, Investigation

PRN: Conceptualization, Writing-Review and Editing, Supervision

CYT: Writing-Review and Editing